Novel atomistic simulation methodology to characterise pore connectivity in porous carbon for energy storage and conversion devices

Ayush Khaitan[a], Ayush Owhal[a], Inturi Ramesh Chandra[a], Manikantan R. Nair[a], Sachin U. Belgamwar[a], Radha Raman Mishra[a], Saurav Goel[b,c] and Tribeni Roy[a,b*]

[a]Birla Institute of Technology and Science Pilani, Rajasthan 333031, India
[b]London South Bank University, 103 Borough Road, London SE1 0AA, UK
[c]University of Petroleum and Energy Studies, Dehradun 248007, India

*Corresponding author: tribeni.roy@pilani.bits-pilani.ac.in

Abstract

Pore architecture in porous materials is an important characteristics to determine energy and power densities of energy storage and conversion devices. Characterization techniques, such as BET, BJH, DFT, etc. either overestimates the data or is computationally expensive. To the best of authors' knowledge, no known existing techniques are present that can measure pore interconnectivity for exclusively microporous carbon. We utilised the power of MD simulation to provide pathway for experimentalists in developing techniques for measurement of pore interconnectivity. A systematic exploration of quenched molecular dynamics (QMD) simulations followed by a thorough characterization for understanding the pore architecture of electrode structures with varying pore sizes was performed. We have developed a new sphere pore modelling technique for the identification of pore interconnectivity based on throats that will allow ions to move in and out of the pores during charging and discharging respectively. New parameters, namely coordination coefficient and throat aspect ratio which quantifies networking and homogeneity of the pores and throats, respectively, were introduced. Decreasing the annealing temperatures, it was observed that the coordination coefficient increased by 18.5 % and throat aspect ratio decreased by 2%. The proposed method and outcomes of this study may help experimentalists in developing new characterization technique particular aimed at estimating pore connectivity.

Keywords: Molecular dynamics, Energy storage, Porous materials, BET, Micropores, Pore interconnectivity

1. Introduction

Modern life is highly dependent on the widespread applications of electronic gadgets, and there is an ever increasing need to find newer ways to supply power at low-cost with high power density for a longer duration [1–3]. Carbon-based materials with different structures such as activated carbon, carbon nanotube, fullerene, graphene, carbon aerogel etc. are an indispensable form of materials with enormous applications including energy storage, energy conversion, catalysis, electronics and many more [4]. Tuneable porosities in these carbon-based materials are gaining research interest due to their high surface area and adsorption applications for energy, environment, and recycling [5,6]. Porous carbon materials have also own high applicability to hydrogen storage due to their high surface area [7–10].

Porosity in carbon-based materials contain pore cavities and the interconnectivity of these pores' eases ion transfers and their adsorption on these materials, which is an essential property for their use as electrodes in energy storage and conversion devices such as metal ion batteries, supercapacitors, fuel cells etc. and can affect their charge-storing capability [11–13]. The porous space is a continuity of absence of solid matter nested in the continuity of solid matter [14]. The available interconnected pore areas and the number of solvated anions and cations that can transfer from the electrolytic solution may affect the capacity of the device [15]. These pores play an important role by creating more surface area in the electrodes. According to the International Union of Pure and Applied Chemistry, USA (IUPAC) [16], porous materials are classified according to the size of the pores that constitute them, and the three main classes are micropores ($< 2\ nm$), mesopores ($2 - 50\ nm$) and macropores ($> 50\ nm$).

Porous structures generally will be bi-modal or multi-modal i.e. more than one class of pores will always be present such as combination of micro and meso-pores in the structure [17]. This makes them essentially irregular and complex in their forms. Detailed insights into the pore architecture are extremely important in order to predict their applicability for applications stated above [18]. However, reliable characterization techniques of such complex porous networks are extremely challenging and are still considered a major challenge. The most important parameters that are usually required from high energy density of point of view in energy storage and conversion devices include pore size distribution (PSD), pore volume, specific surface area (SSA) and pore interconnectivity [19,20]. Gas physisorption equilibrium isotherms of nitrogen, argon, or carbon dioxide adsorbates are the most commonly methods used for characterizing pore

architectures [21,22]. Brunauer-Emmett-Teller (BET) is one of the most commonly gas physisorption methods for evaluating SSA of porous materials [23,24]. However, BET often overestimates surface areas and is, therefore not highly accurate [25]. Barrett-Joyner-Halenda (BJH) and Density Functional Theory (DFT) are exclusively used for estimation of PSD. Accuracy of DFT is higher as compared to BJH [26]. X-ray micro-computed tomography (XMCT) has also been used to capture insights into porous carbon structures of materials [27,28]. XMCT scanning provides information of interfacial morphology and porosity of catalyst layers of carbon system [29]. All these processes described will provided one or more parameters and the rest will be derived based on post processing of the data. One of the most important parameter i.e. interconnectivity of pores is very critical in developing high energy and power densities in energy storage and conversion devices. This parameter is however not possible to be determined with the current available techniques. For developing numerical models in batteries/supercapacitors, this pore connectivity is termed as tortuosity that takes into account the transport of ions in the porous materials [30]. For all purposes, this tortuosity factor is considered a constant value; while in reality, the pore connectivity will change across the length and thickness of electrodes.

Molecular dynamics (MD) simulations have been found most relevant approach that allows atomic level studies that can be used to get a visual understanding of atomic interactions happening throughout various reactions like in this case of pore formation, ion transport in the electrodes, double layer formation, etc. [31,32]. Atomic-level studies can be highly useful in studying molecular properties, structure, and structure-property interaction [33]. MD simulation works by simulating atoms and molecules in a virtual environment to study various aspects like physical and chemical interactions based on their nature [34]. In the case of porous carbon electrodes, many such simulation studies have been conducted to understand the behaviour of carbon atoms and their possible structures. He et al. [35] investigated the graphitization mechanism during the thermal process using molecular dynamics simulation by which they could understand the temperature dependence on pore formation. Bo et al. [36], used molecular dynamics to study how doping the electrode materials would help in increasing the specific surface area, and thereby increase the specific capacitance.

In this paper, our main focus is to utilise the power of MD simulation technique to provide pathway for experimentalists in developing techniques for measurement of pore interconnectivity in electrodes for applications in energy storage and conversion devices. We have systematically

explored the use of quenched molecular dynamics (QMD) simulations followed by a thorough characterization for understanding the pore architecture of electrode structures with varying pore sizes. We have developed a new sphere pore modelling technique for the identification of pore interconnectivity based on channels that will allow ions to move in and out of the pores during charging and discharging respectively. We have also simulated BET method to analyse the surface area of the simulated porous carbon.

2. Method and simulations

2.1 MD modelling

2.1.1 Potential function

The interatomic potential for carbon-carbon interactions in porous carbon structures refer to the mathematical model that describes the interactions between the carbon atoms. The potential for a material with a highly ordered and crystalline structure may be different from that of a material with a more disordered and amorphous structure. In the previous study [37], we used an adaptive intermolecular reactive empirical bond-order (AIREBO) potential by Stuart et al. [38] based on the second-generation REBO where long-range interactions are described by a Lennard-Jones term with a switching function to restrict their effect at short distances.

Gaussian Approximation Potential (GAP) is a more general-purpose potential than AIREBO that can be used to model a wide range of systems, including both carbon-based and non-carbon-based molecules [39]. GAP is recently developed by Deringer and Csányi [40] for liquid and amorphous carbon that showed close-to- density functional theory (DFT) accuracy where kernel-based machine learning is employed instead of a classic empirical functional form. GAP is a category of interatomic energy models that can be automated from data that combines the energy and energy received by atoms, found in quantum mechanical studies. A hierarchical set of two-, three-, and many-body structural descriptors are also included in the GAP potential. Fitting structural and thermodynamic features to quantum DFT data yields parameter sets.

To ensure that GAP can accurately simulate the graphitization process, we performed some benchmark simulations as summarised in ***Fig. 1***. It is well known from experimental and density-functional theory (DFT) studies that the sp^2 fraction of the carbon system increases linearly with density, and hence this relationship represents one of the simplest tests of the transferability of a carbon potential. The relation between sp^2 fraction and density of carbon system is reliable in

assessing a potential. ***Fig. 1*** shows the sp^2 fraction vs. density for both the potentials studied in this work. At low densities both potentials have sp^2 fractions comparable to each other, but as the density increases, significant deviations occur. We note that the sp^2 fraction values were 64.2% higher than AIREBO potential at density value of 0.95 g/cm^3. The result of this comparative study shows that for all values of selected densities, GAP has higher sp^2 fraction values.

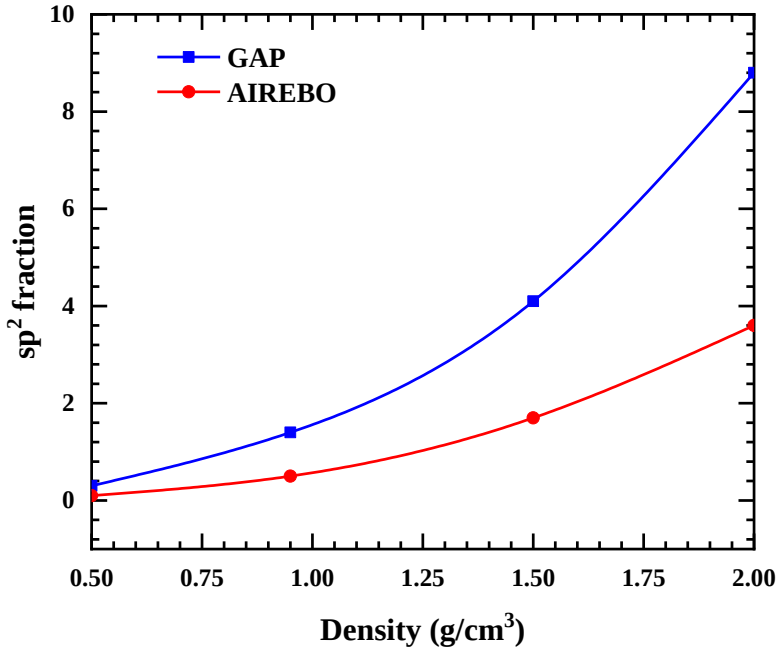

Fig. 1: sp^2 fraction vs. density plots for AIREBO and GAP interatomic potential.

2.1.2 MD parameters

LAMMPS simulation package (version 24-Mar-2022, Sandia National Laboratory, Albuquerque, NM, USA) [41] was used for QMD simulations. A fixed cuboidal box of dimension $20.3\,nm \times 10.1\,nm \times 10.1\,nm$ containing *100,000* carbon atoms with periodic boundary conditions was used to simulate a system to maintain a density of 0.95 g/cm^3. The canonical (NVT) ensemble is used to control the temperature [42], and all computations are done with a timestep of 0.5 fs. Random placements provide the system a fluid-like beginning state to offset biases coming from an ordered initial state at 10,000 K. The system is first cooled from 10,000 K to 300 K with varying quench rates for different cases. We employ an annealing methodology in which the simulation temperature is maintained at a single value for a long period. Our methodology mimics

the experimental synthesis of TiC-CDC [1]. The sublattice is annealed for 30 ps at temperatures of 8000 K, 6000 K, and 4000 K to form three different cases of porous carbon system, namely AT8000, AT6000 and AT4000 respectively. This annealing stage is critical for transitioning a high-energy quenched structure to a relaxed and equilibrated structure. The intermediate quench rates employed to form the carbon systems are shown in ***Fig. S1***. After obtaining the MD trajectories for all the cases, we used OVITO [43] to render and analyse the structural images and morphological properties. Coordination analysis was performed to gather the *sp*, sp^2, and sp^3 structural motifs information using a cut-off distance of 1.735 Å for hexagonal ring bonds, which fully encloses the first-neighbours shell for porous carbon [44]. Furthermore, to study the graphitic ribbon quality, radial function distribution (RDF) analysis was carried out.

2.2 Porous structure characterisation

Measurement of nitrogen or argon adsorption isotherms at their liquid phase temperature and XMCT image analysis are widely used in characterising porous carbon structures [21]. Using an idealised geometric model of the pores, BET and DFT analysis of the isotherms provide an estimate of SSA and PSD of the material [45]. A central weakness in this approach is the use of an oversimplified pore model that neglects pore connectivity, coordination, and heterogeneity. Such pore models may give a reasonable account of adsorption isotherms; however, often provide qualitatively incorrect heats of adsorption and are particularly poor for predicting diffusion rates [46]. Once developed, SSA, porosity, and PSD of these model materials can be determined using probe molecules and statistical and geometric analysis. Knowledge of the PSD is particularly important since it determines the size of molecules that can be accommodated, selectivity in separations and reactions, etc. A common difficulty in characterising these realistic model materials is that the analysis to get the PSD is computationally very demanding, and currently this is a limitation in the application of these models. In this subsection, we report a new sphere pore method for rapid calculation of the PSD that removes this difficulty.

2.2.1 Sphere pore model

The sphere pore model is based on the assumption that the pores in the carbon structure have a spherical shape and involves measuring the size of the pores and then using statistical analysis to calculate the PSD. The pore size at a given point can be defined as the largest sphere that

encompasses the given point without overlapping the neighbouring wall atoms. A schematic in two dimensions is shown in ***Fig. 2***. The circles are the various spheres that can be constructed through a pore channel without overlapping the wall atoms. The proposed approach is explained in a flowchart as shown in ***Fig. 3.***

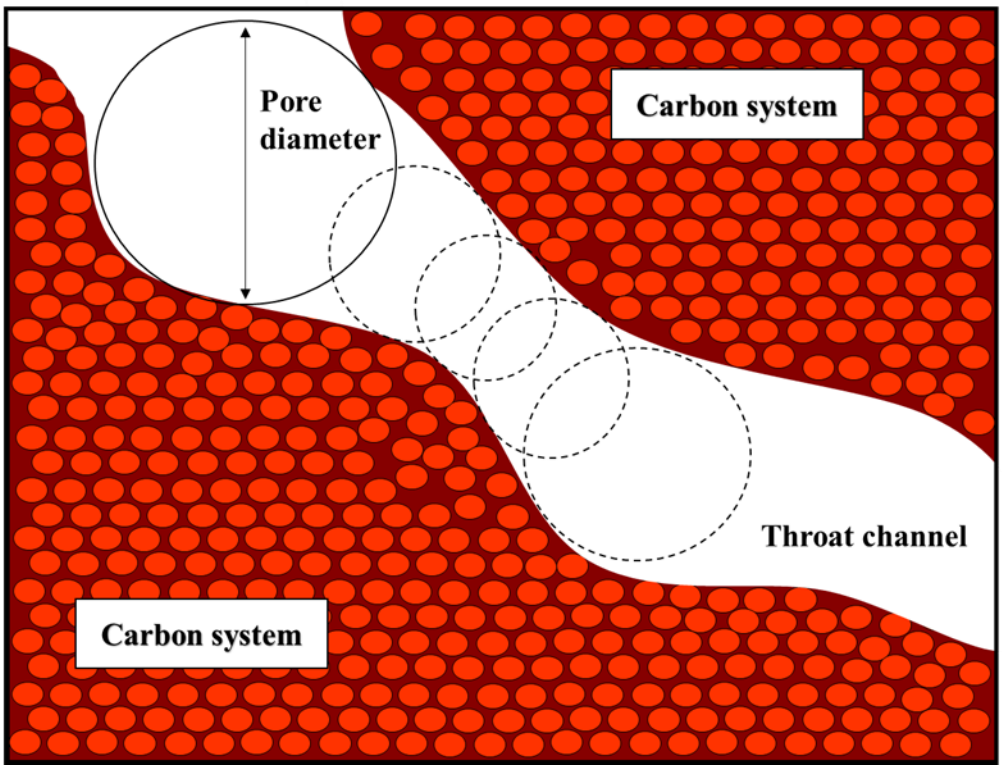

Fig. 2: Schematic for sphere pore fitting across porosity of carbon system.

The first step is to create a database of all eligible spheres with a diameter of over 0.154 nm into the carbon structure array C. A typical carbon hexagonal ring has a side length of 0.154 nm and a central void space to fit a sphere of diameter 0.154 nm [ref]. During calculation, a total of *n* sample points are taken where the pore sizes are to be measured and stored in the array C. Let *R* be the radius of the enclosed sphere, s_i is the distance between *O* and the centre of the i^{th} sphere, this can be written as,

$$R(O) = MIN[s_i] - r, \qquad i = 1, 2, \ldots, n. \tag{1}$$

Subsequently, to find the pore size R_i for pore *i*, the database was traversed for overlapping spheres inside pore *i* and kept only the largest among them.

Although the remaining pores in array C can provide the partial porosity of carbon structure, it results in most of the voids unfilled by pore spheres. To mitigate the partial filling of the carbon system, we provide an iterative method to capture all the void spaces. In this method, the remaining pores were again subjected to the first step as a modified array, i.e. creating a database of all spheres which does not overlap neither any carbon nor any existing pore. These iterations were carried out till no new spheres were obtained. The final result was an array of non-overlapping pores which completely filled the void space of the concerned carbon system. The pore size distribution for different cases of carbon systems were calculated by the obtained radii of best-fitted sphere pores.

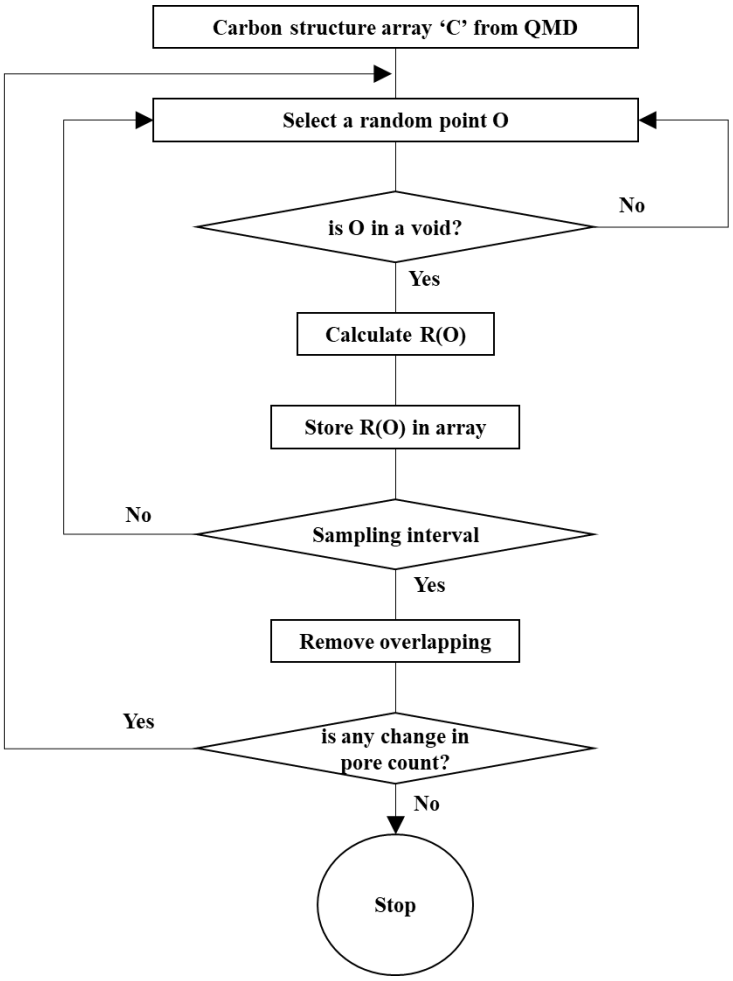

Fig. 3. Proposed procedure for sphere pore method. Here, O is a random sampling point inside the model volume, R(O) is the particle radius, respectively. C is the array containing information about coordinates and radii of carbon and pore spheres.

2.2.2 Pore coordination study

The geometry and topology properties of the complex pore structure are vital for revealing the fluid transport properties in pore space. An equivalent pore network model of interconnected pores can reproduce the complex pore structure of the porous medium [47]. The purpose of pore network extraction is to tessellate the pore system into pores and throats. Spheres and cylinders usually represent the pores and throats, respectively. In this way, geometry and topology properties can be analysed in the pore network [48]. This approach can produce representative networks that make reasonable estimates of pore geometry and transport properties. These approaches may not be able to generate a unique representation of the pore system due to inherent approximations and dependency on image resolution. This pore network extraction algorithm can decrease the uncertainties in conventional network modelling predictions introduced due to the oversimplification of complex pore geometries encountered in porous materials.

In this paper, pores and throats were identified using coordination analysis of the sphere pore model generated in the above section. The degree of pore interconnectivity is an essential property of the porous carbon structure in the study. Coordination analysis is a practical approach to quantify the degree of connectivity of the porous network. The coordination number of a pore is a representation of the number of different pore spheres connected to the pore in concern. An ideal model with uniform cross-sectional pore channels after the application of the sphere pore method would contain pore spheres of uniform radii packing the entire void space. A 2D representation of this is shown in ***Fig. 4***. In such a case, each sphere has a certain coordination number, i.e., the number of other directly connected spheres. Sphere pores situated at the middle of a channel would be surrounded by two other spheres, one in front and the other at the rear. Hence, the coordination number for this middle pore is two. A similar sphere, situated at the junction of multiple channels, would be connected to a higher number of spheres. This sphere at the junction, mentioned here onwards as a node, has a coordination number equal to the number of coinciding channels. ***Fig. 4 (a)*** explains this concept with a few examples. Spheres numbered two are situated in the middle of a channel. Whereas spheres numbered otherwise are at junctions for as many channels. A database of an ideal case involving the coordination data for all pores provides an excellent approximation of the degree of connectivity in the porous carbon.

A real system, however, contains pore spaces which are uneven in their cross-sectional area. Such a system would contain pore spheres of varying radii. While assigning a coordination

number to each pore, a spatial correlation between the coordination number and pore size needs to be carefully considered. From ***Fig. 4 (b)***, it can be found that the coordination number increases with the increase of the pore size. As a result, it is suggested that the larger coordination numbers should be assigned to larger pores. After assigning coordination to each node, one can find that the coordination number for the larger pore is much greater than the assigned coordination number. Hence a dilution process has to be applied to eliminate excess coordination numbers. Three operations should be used in the dilution process:

1) Choose the pore throat with the highest priority. The priority of each pore throat can be determined by the formula:

$$P_{ij} = 1 + F(s_i)F(s_j). \tag{2}$$

where $F(s_i) = 1 - n_i/a_i$, PB_{ij} is the priority of bond connecting node i and j, n_i is assigned coordination number for node i, a_i is the available number of bonds connecting node i.

(2) Choose the bond with the shortest length. A bond length greater than 0.154 nm. i.e., the diameter of a carbon atom, is removed from the original count. This is to eliminate the possibility of a graphitic sheet being present between the two pores.

(3) Choose the bond connecting the pore to an equivalent comparable-sized or a larger-sized pore.

For the above three algorithms, the priority of each algorithm is decreasing. During the dilution process, some nodes may be isolated from the neighbouring nodes, and these nodes will lead to numerical problems during the simulation of flow through the network. As a result, an effort was made to remove the isolated node or cluster from the network. Based on the above description of the algorithm, it can be found that the equivalent network can match the main geometrical information of pore structure including PSD and correlation between pore size and throat size. After the dilution process, the equivalent network can match the coordination number distribution which contains the main topological information of the pore structure. Then, this equivalent network has the flexibility to match the geometrical and topological features of the pore structure. ***Fig. 4 (b)*** shows a 2D representation of a system with pore spheres of varying radii. The

coordination numbers of these pores have been diluted with the use of the above-mentioned three algorithms. Each sphere has its diluted coordination number mentioned on it.

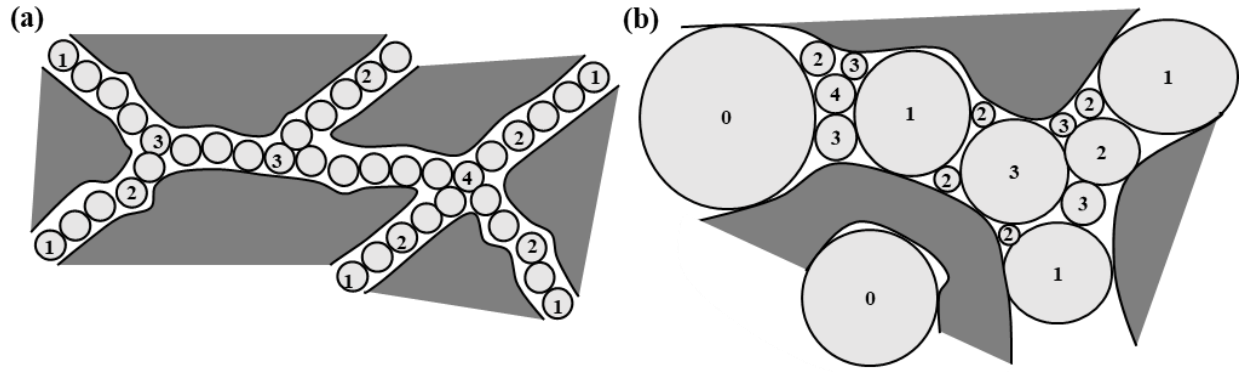

Fig. 4: 2D representation of a system of sphere pore model with assigned coordination numbers for different neighbour bonding conditions. (a) Ideal case of uniform pore channel cross sectional area and shape, (b) Realistic case with varying pore channel cross sectional area.

2.3 Adsorption isotherm analysis

Additionally, an atomistic modelling used for nitrogen adsorption isotherm [49], and the obtained data was post-processed to calculate SSA of the porous carbon structure. Nitrogen gas (adsorbate) at 77K was routed through the carbon system. In the process, nitrogen was adsorbed onto the surface of the porous carbon structure as a result of interactions between carbon atoms and nitrogen molecules, resulting in multilayer nitrogen gas adsorption over the porous carbon structure. Once the nitrogen adsorption was completed over the porous carbon structure, the BET surface area was calculated using the monolayer of nitrogen that was adsorbed into the surface of the porous carbon. The equation that was used to calculate the BET surface area is shown below:

$$A = N_m \cdot A_m \cdot N_{av}. \tag{3}$$

where A is the BET surface area, Nm is the monolayer of nitrogen adsorbed, Ac is the cross-section of the adsorbate (16.2 $Å^2$ for N_2) [50], Nav is the Avogadro number. The adsorbed monolayer of nitrogen was calculated using the BET equation [51] is given as,

$$\frac{\left(\frac{P}{P_o}\right)}{N\left[1-\left(\frac{P}{P_o}\right)\right]} = \frac{1}{N_m \cdot C} + \frac{C-1}{N_m \cdot C}\left(\frac{P}{P_o}\right). \tag{4}$$

where P/P_o is the relative pressure with P_o = 1 bar, N is the total nitrogen adsorbed, and C is the BET constant. BET equation could be graphically plotted to obtain the adsorption isotherm.

3. Results and Discussion

A QMD routine was used to generate atomistic models for porous carbon structure [52]. The quenching temperature varies from 10,000 K to 300 K with varied annealing temperatures and obtained thermal responses are shown in ***Fig. S2***. ***Fig. 5*** **(a)** compares the simulation structures of all the three cases of different annealing temperatures, and the images provide qualitative analyses of sample morphology and structural properties. A comparison of image insets of ***Fig 5 (a)*** shows that the carbon mesh becomes dense on increasing the annealing temperature. At higher annealing temperature of 8000 K, the simulated structure is essentially fully disordered with uniform and relatively small pores. The curved structures were seen in the case of an annealing temperature of 4000 K, and larger pores start to develop. For cases 2 and 3, the graphitic ribbons are longer and straighter compared to case 1. For case 3, the simulated carbon structure found stacked graphene nanosheets. However, stacking was absent in cases 1 and 2. The results complement the previously reported experimental (TEM) and simulation study of Tomas et al. [52]. At the lowest annealing temperatures, the simulated structures contain a large number of layers, though not as many due to the finite size of the simulation box. In our simulations, to mimic an experimental temperature of 1800 K, there are two possibilities: (i) a simulation time of 200 ps with a starting temperature of approximately 10000 K, or (ii) a very long simulation of the order of microseconds. The former is beyond the melting point and hence impossible, while the latter is computationally too expensive. As a compromise, we anneal at different temperatures for 40 ps. Despite this approximation, there is a good qualitative agreement between previously reported experimental results and simulation [52], with the simulations reproducing large stacks of graphitic ribbons.

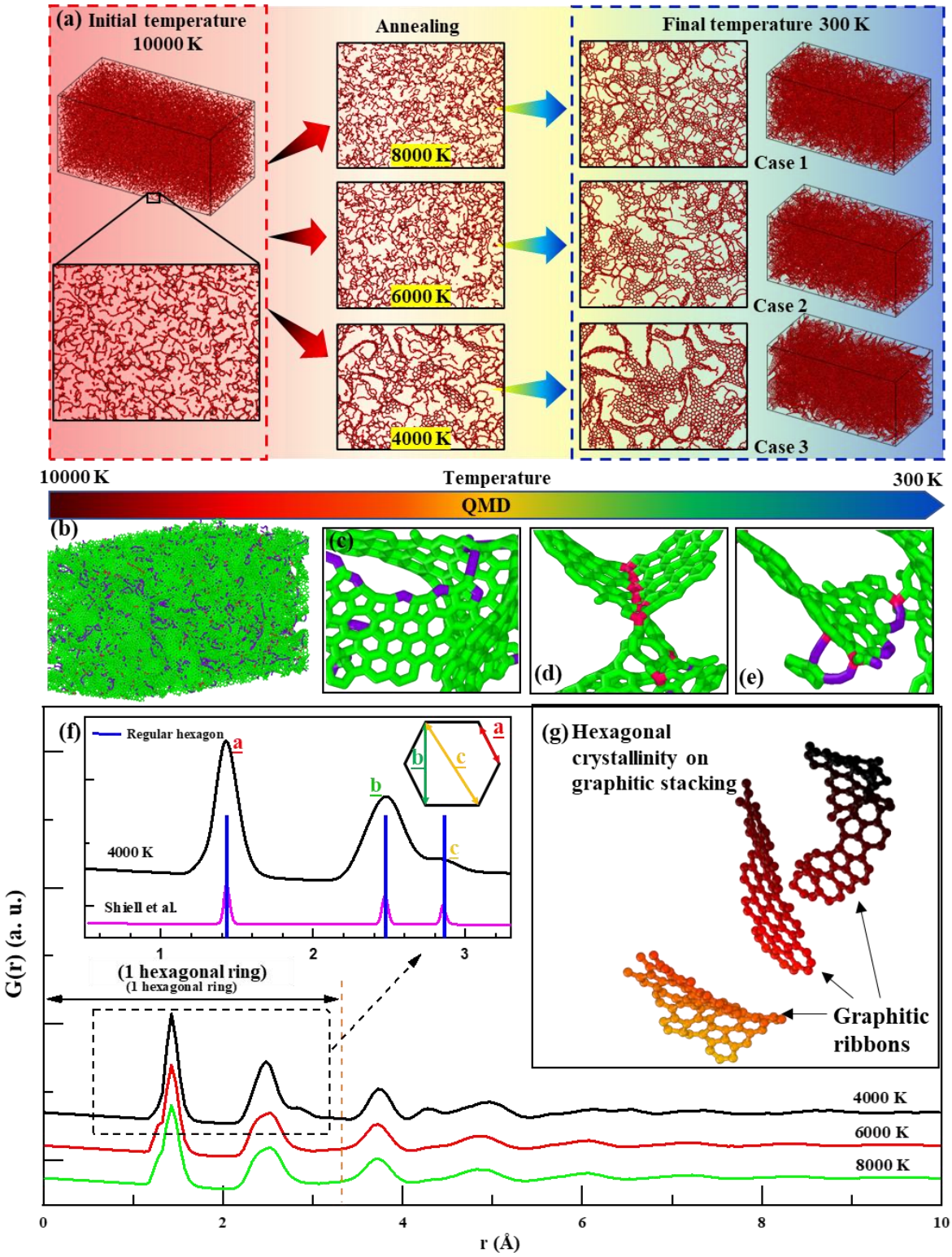

Fig. 5: (a) Obtained carbon systems for different annealing cases, (b) *representation of spn motifs in C-C bonds* (c) *sp* motifs, (d) sp^3 motifs, and (e) combined *sp* and sp^3 motifs for AT4000. (f)

Reduced RDF analysis for AT4000, here, inset show the significance of a, b, and c peaks for the formation of hexagonal rings compared with standard and experimental graphs reported by Shiell et al. [53].(g) Obtained hexagonal crystallinity with the stacking of graphitic ribbons.

3.1 Qualitative analysis of carbon structure

The cross-sectional morphology of the quenched carbon structures for the case of annealing temperature of 4000 K has been studied for qualitative validation of honeycomb nanostructure formations (***Fig. 5a***). Clearly, most of the carbon in these samples is made up of curved graphene fragments with predominantly sp^2 bonding, quantified in ***Table 1***. These fragments assemble into three-dimensional networks, where edges containing *sp* motifs and planes can become interlinked through sp^3 motifs (refer ***Fig. 5 (b-e)***), which is the same role played by interstitial defects in graphite. One of the distinctive characteristics of these carbon structures is the typical nano structuring of the various tangled graphitic ribbons, as shown in ***Fig. 5 (b-e)***. Due to their importance for emerging and established applications, PSD merit further discussion. We provide an in-depth analysis of pore morphology later in this section. Consistent with the extremely high sp^2 fraction reported in ***Table 1,*** our results show a predominance of hexagonal ring motifs. However, many of the unstable defective rings remain after QMD for graphitization to 300 K, for all the cases studied here. In order to ensure the validity of the carbon structures obtained here, it is of great importance to assemble the evidence by calculating several key structural indicators and comparing them with previous experimental data. Radial distribution functions, G(r), are direct tools to characterise the similarity between simulated and experimentally synthesised structures. Radial distribution functions, G(r), are direct tools to characterise the similarity between simulated and experimentally synthesised structures [54], can be represented as follows,

$$G(r) = 4\pi\rho_{at}[g(r) - 1]. \quad (5)$$

where ρ_{at} is the atomic density in, e.g., atoms/Å^3

The reduced RDF G(r) commonly used in experiments is related to the RDF g(r) most often reported in simulation work (eq 6). ***Fig. 5 (f)*** presents the G(r) of the reference experimental data and our simulated carbon samples. We take the 0.95 g/cm^3 model structure as the closest to carbide-derived carbon (CDC) models [55], because of the similarity in mass density. The G(r) for each sample is shown in ***Fig.***

5 (f). Some small oscillations remain as a consequence of the scaling process, but decrease in intensity with an increase in the radius, *r*. The first three peaks of the carbon samples spectrum have been magnified and are displayed in the inset in ***Fig. 5 (f)***. The locations of the first three peaks representing the spacings within a six-membered ring are remarkably similar for all cases. These three peaks are labelled *a*, *b*, and *c*, where the distances they represent correspond to the interatomic spacings within a six-membered hexagonal ring. These peaks give an idea of the typical regions in a graphitic sheet free of defects, i.e., made of hexagonal rings only. The relative intensities of peaks for all cases are similar to the experimental G(r) spectra of CDC, reported by Thompson et al. [54]. The first three peaks at 1.42, 2.52 and 2.87 Å correspond to neighbours in a hexagonal ring and peaks at 3.77, 4.32, and 5.02 Å correspond to the location of carbon atoms in neighbouring rings. However, significant peak asymmetry and broadening observed at the third and further peaks do indicate the presence of non-hexagonal rings. It is observed that the intensity of peaks increased, and the broadening of peaks decreased on reducing the annealing temperature. It is possible that this is caused by the higher level of impurities in higher annealing temperature samples, causing defects within the hexagonal crystallinity of graphene nanosheets, effectively lowering the medium-range order. In this sample, the graphitic sheets are stacked locally similar to a graphite crystal encompassing multi-layers, as shown in ***Fig. 5 (g)***. These observations are consistent with both the Raman results and TEM analysis reported Shiell et al. [56].

The quantitative characterization includes a sphere pore model for pore volume, PSD, and pore interconnectivity. Subsequently, simulated BET analysis for SSA.

3.2 Sphere pore analysis

One of the critical characteristics of porous carbon structures is their porosity, which is defined as the empty volume contained within the structure. Therefore, the characterization of porosity and pore structures in our computational samples is a central part of this work. Experimentally, it has been observed that the total porosity is similar for all temperatures, while the distribution of pores is temperature-dependent [37]. ***Fig 6 (a)*** shows the partial carbon system for *Case 3*. This system was further subjected to the proposed sphere pore method as already discussed in *Sections 2.2.1 – 2.2.2*. The pores of best fitting size are represented as grey spheres. Applying this method, the structures yield a porosity between 20.4% and 25.6%. In carbon systems, micropores are obtained, which were created by voids between stacked graphitic ribbons (refer ***Fig 5 (g)***).

Pore size distributions of QMD samples are shown in **Figure 6b.** Consistent with previous QMD studies [57], the pore size and dispersity increase with slower quench rates. PSD graphs behave similarly to normal distributions. We note that from literature [58], the experimental characterization results demonstrate a strong predominance of sub-nanometre pores, which in our cases occurs as a peak at a pore diameter of 0.4 nm. A small shoulder at 1–1.1 nm in cases 2 and 3 as the largest pores are located between stacked graphene layers at lower annealing temperatures.

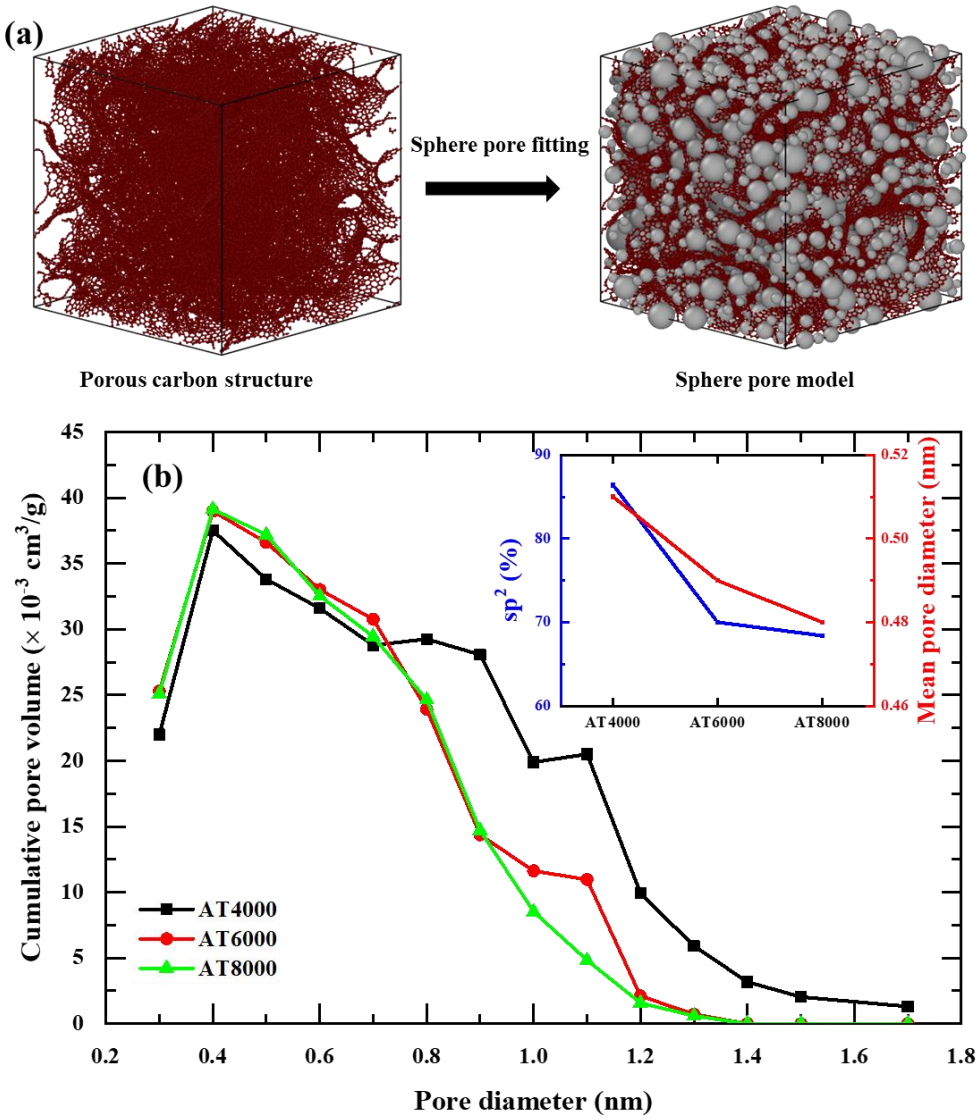

Fig. 6: (a) Developed sphere pore model for AT4000 carbon system, (b) Cumulative PSD function with an inset comparison of sp^2 fraction (%) and mean pore diameters for different annealing cases.

We can clearly see, as expected, that the PSDs shift to smaller mean diameters with increasing annealing temperature, as represented in inset of ***Fig 6 (b)***. The mean pore diameters for different cases are 0.48 nm for *Case 1*, 0.49 nm for *Case 2*, and 0.51 nm for *Case 3*. The graphitic ordering is represented by sp^2 percentages; the graphitic sheets provide open spaces for ions to settle on. A higher value of sp^2 percentages in *Case 3* (86.4%) indicates a more ordered structure in terms of graphitic ribbons compared to the other two cases (*Case 1*- 68.4 %; *Case 2*- 70%). As a consequence, mean pore diameters increase along with graphitic ordering is coherent with the current discussion. These results highlight the effectiveness of the proposed method in characterising the pore space and revealing the effects of underlying structural changes. It should be pointed out that our PSD analysis is based on a spherical approximation to pores and highly sensitive to small changes in the pore diameter.

3.2.1 Pore network analysis

The coordination number that can be obtained from pore network extraction has an essential impact on transport properties [48]. A pore body coordination number can be obtained by counting the number of throats that directly connect the pores to their neighbouring eligible pore bodies. A higher value of the coordination number means that the pore is well connected, i.e., a typical pore connects directly to a large number of other pores.

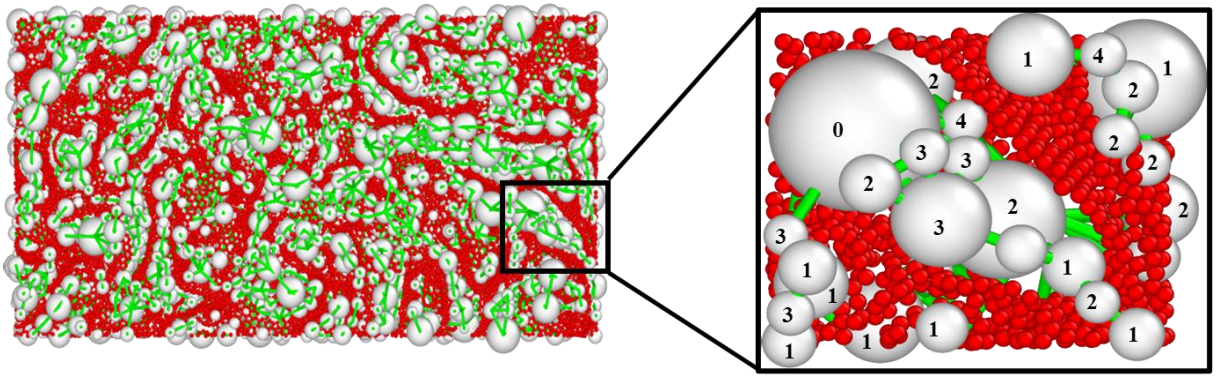

Fig. 7: Coordination analysis for AT4000 carbon system. Red and white spheres represent carbon atoms and pore spheres respectively. Green bonds depict the coordination throats between two pore spheres. (inset shows the magnified view of selected pores with their coordination number).

Fig. 7 depicts the coordination of pores within a sliced section of AT4000. The carbon atoms are represented as red spheres, pores of different diameters are shown with white spheres and throats as green bonds. The inset alongside shows a magnified view of the fitted pores and

throats with calculated coordination numbers for each pore. This analysis shows the interconnectivity across different pores in an amorphous carbon structure, which is an important factor in determining its performance in energy storage and conversion devices.

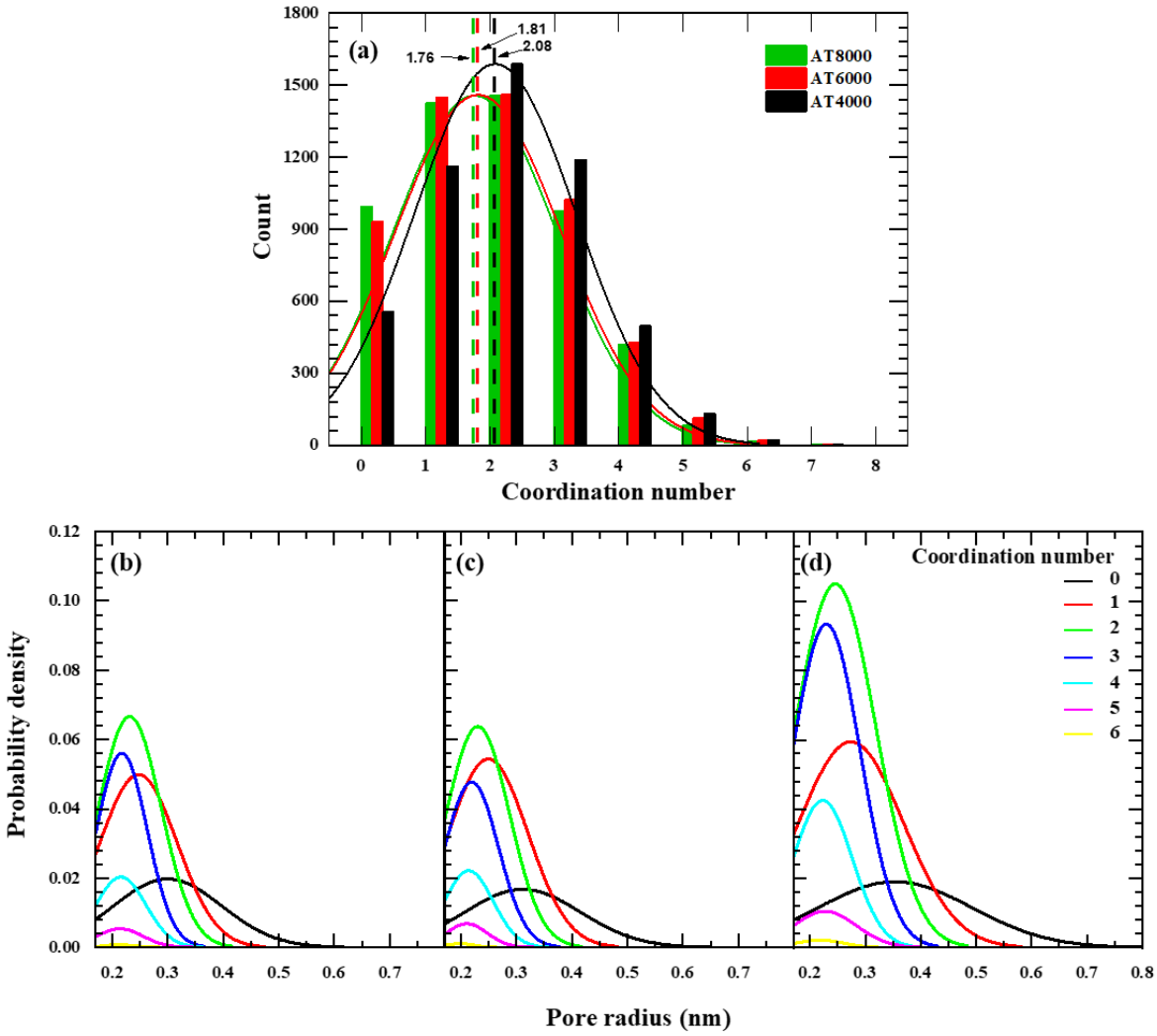

Fig. 8: **(a)** Coordination number distributions and the mean coordination number of the three carbon samples. (b-d) Probability distribution of sphere pores as a function of pore radius for each coordination number. (b) For case AT8000, (c) For case AT6000, (d) For case AT4000.

Fig. 8 (a) presents the coordination number distributions and their mean coordination number of the three carbon samples. The distribution of the calculated coordination number ranges from a minimum of 0 to maximum of 8. AT4000 shows a mean coordination number value of 2.08, which is largest among the annealing cases. The mean coordination number of AT4000 is

15.3% higher than that of 1.76 for AT8000. The distribution of radii for each individual coordination number is visually represented in ***Fig. 8 (b)***. The graph is extracted for the carbon samples, each containing total pores ranging from 5153 for AT4000 to 5461 for AT8000 with varying diameters. As evident from the graph, larger pores have lower coordination numbers, whereas smaller pores dominate the curve for larger coordination numbers. AT4000 shows highest peaks for all coordination numbers greater than 2 compared with AT6000 and AT8000. It is evident from coordination analysis that pores participating in network channels have higher coordination numbers,

Wider interconnected throats facilitate higher permeability in a porous carbon system. Throat width is directly proportional to the diameters of its associated pores. Thus, the coordination coefficient is calculated to exaggerate the weightage of pore diameter in coordination analysis. A weight factor is associated with pore radius to interpret the true networking of a particular carbon sample. Coordination coefficient is a promising way to quantify networking in carbon samples. It is a weighted average of coordination numbers for all the pores. We calculated the coordination coefficient characterising pore connectivity with the following equation,

$$\zeta = \left(\frac{1}{N} D_{avg} \right) \sum_i (C_i \cdot d_i). \tag{6}$$

where N is the total number of pores, D_{avg} is the average diameter of pores, C_i and d_i are the coordination number and diameter respectively for pore i.

Coordination coefficient was compared for all three carbon systems. The average network statistics for the coordination coefficient are displayed in ***Table 1.*** There are noticeable changes in the coordination coefficient between the low porosity group (AT8000) and the high porosity group (AT4000). We can see that AT4000 has the largest coordination coefficient of 1.921, indicating that the pores and throats are well connected. AT8000 has the least coordination coefficient of 1.629 since the sample only present a total porosity of 20.4% and a large number of pores are sealed by diagenesis. The relatively low coordination coefficient is due to a large number of pores with poor connectivity. Coordination coefficient and pore connectivity, however, describe different properties and should not be confused. Pore connectivity is a measure of the branching of pores in a skeletonized representation of the interconnected network. Coordination coefficient refers to the compartmentalised representation of the porous space and measures the number of pores with which a given pore shares throat voxels [48,59].

Table 1. Coordination Fractions of sp^n ($1 \leq n \leq 3$) bonds, coordination coefficient, throat aspect ratio, and BET surface area obtained for different annealing cases.

Parameter / Cases	sp^n ($1 \leq n \leq 3$) fraction			Coordination coefficient	Throat aspect ratio	BET specific surface area (m^2/g)
	sp (%)	sp^2 (%)	sp^3 (%)			
AT8000	30.3	68.4	1.3	1.62	1.172	464
AT6000	28.2	70	1.6	1.66	1.172	906.7
AT4000	12.3	86.4	1.3	1.92	1.148	1485

3.2.2 Throat aspect ratio

Throat aspect ratio is an appropriate parameter for characterising the degree homogeneity of the pore system. In this paper, the global aspect ratios have been validated, using the inscribed radii given in the network data files. The global aspect ratio is the ratio between the average of the pore sizes of two pores sharing a throat and the length of that throat. The average throat aspect ratio (τ) was calculated as follows:

$$\tau = \left(\frac{1}{N}\right)\sum_i \left(\frac{L_i}{D_m}\right). \quad (6)$$

Where N is the total number of throats, L_i is the length of throat i and D_m is the average diameter of the two pores connected to pore i.

The throat aspect ratio was an adopted index to analyse the differences concerning the dimension of pores and pore-throats. As shown in ***Table 1***, the throat aspect ratio ranges from 1.14 to 1.17 for AT4000 and AT8000, respectively. There are noticeable changes between AT4000 and AT8000. Compared to the AT4000, AT8000 samples show a higher AR, indicating some pores exist in the form of bottlenecks. The large value of this parameter may be an important factor leading to poor connectivity in carbon samples. The feature of large-pore spaces and small throats

is one of the main characteristics, which distinguishes porous carbon structures from conventional carbon structures.

3.3 BET adsorption isotherm analysis

In BET adsorption isotherm process, the relative pressure (P/P^o) of the adsorbent (here, nitrogen) is directly related to their adsorption on porous carbon structure [60]. Thus, analysing the BET adsorption isotherm aids in calculating the surface area of the porous carbon structure in relation to the adsorbed volume of nitrogen inside the structure. The BET adsorption isotherm is depicted in ***Fig. 9***. The BET adsorption isotherms of this study are in good agreement with the experimental reported results of Lee et al. [60] and Mistar et al. [61]. MD simulation of BET surface area analysis of porous carbon structure, it was observed that when nitrogen gas was introduced into the porous carbon structure, initially the nitrogen formed a monolayer (a single layer of nitrogen molecules) on the walls, and as the pressure of the nitrogen gradually increased, the amount of nitrogen that filled the porous structure also increased, leading to the formation of multi-layered nitrogen (nitrogen molecules forming multiple layers one over the other) over the structure. Gradually, the porous structure was filled with nitrogen, and the BET adsorption isotherm was plotted. In general, there are six types of BET isotherms available based on the shape of the plot, which in turn, represents the volume of adsorbent that was adsorbed into the porous structure [62].

In this simulation, Type 1 isotherm was found, which shows that the porous carbon structure has micropores. This could be understood from the BET isotherm region, which corresponds to 0 to 0.2 relative pressure. Over this area, it could be seen that the amount of nitrogen that has been adsorbed by the porous carbon is rapidly increasing with pressure Khosrowshahi et al. [63]. This could be due to the presence of micropores, which would increase the surface area inside the porous structure for the nitrogen molecules to interact with, and this may have aided the nitrogen molecules to spread further into the structure, which rapidly increased the adsorbed volume of nitrogen inside the porous carbon structure [61]. It is also observed that, in the relative pressure range of 0.2 to 1.0, the nitrogen adsorption is almost constant because the nitrogen gas's monolayer formation is complete. Now, the nitrogen just builds up layers inside the pores and fills the whole structure. Once the structure was filled with nitrogen, the BET surface area was calculated using the BET isotherm. The calculated BET surface area of the three porous structures

annealed at 8000 K, 6000 K, and 4000 K was found to be 464 m^2/g, 906.7 m^2/g, and 1485 m^2/g, respectively. The results are consistent with the experimentally derived surface area reported by Lee et al. [60] and Mistar et al. [61].. From these BET surface area values, it could be inferred that annealing at a higher temperature could significantly contribute to increasing the surface area of the carbon system.

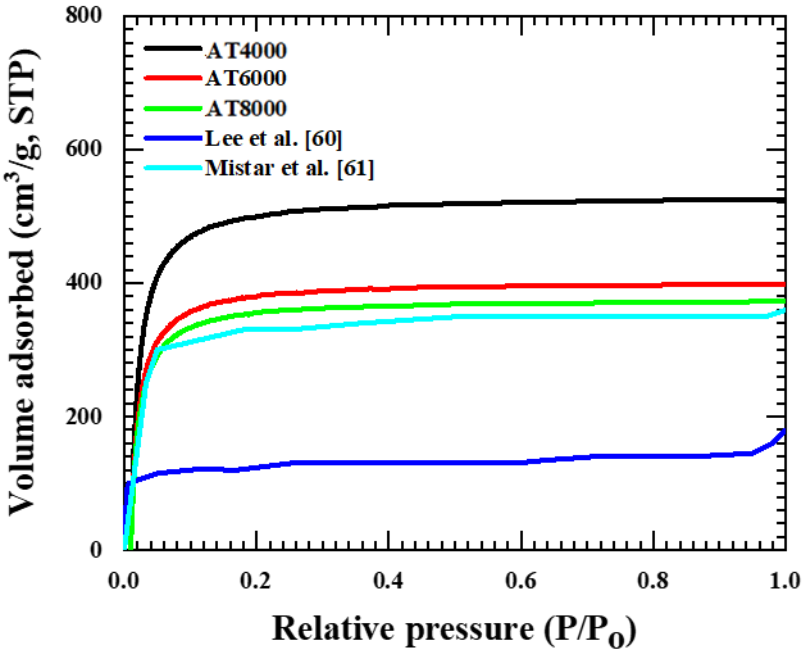

Fig. 9: BET adsorption isotherm for three porous carbon structures. The graph is in the form of a Type I BET adsorption isotherm, which represents the presence of a large volume of micropores. Micropores allow fast initial adsorption of N_2 molecules. Here, results are compared with the reported experimental results of Lee et al. [60] and Mistar et al. [61].

4. Conclusion

We proposed the development of sphere pore method for the characterization of pore connectivity in porous carbon structures simulated by using quenched molecular dynamics. Different annealing conditions were adopted for cooling the carbon system to create different porous geometries. The interconnected throats sequencing is developed through pore coordination analysis. We characterized it for its pore sizes that will allow ions to move in and out of the pores during charging and discharging in energy storage and conversion devices. This paper introduced

new parameters such as coordination coefficient and throat aspect ratio, that quantifies networking and degree homogeneity of the pores and throats in the carbon samples generated using the proposed method, respectively. Decreasing the annealing temperatures, it was observed that the coordination coefficient increased by 18.5 % and throat aspect ratio decreased by 2%. We additionally simulated the BET surface area analysis on simulated porous carbon structures and found that the more micropores are formed at higher annealing temperatures, and the formation of larger graphitic ribbons would lead to 120% increased surface area at lower temperatures. The proposed method and outcomes of this study may help experimentalists in developing new characterization technique particular aimed at estimating pore connectivity.

Author contributions

AK – Conceptualization, Data curation, Formal Analysis, Investigation, Methodology, Software, Validation, Visualization, Writing – original draft, Writing – review & editing

AO – Data curation, Formal Analysis, Investigation, Methodology, Software, Validation, Visualization, Writing – original draft, Writing – review & editing

IRC – Data curation, Formal Analysis, Investigation, Methodology, Software, Validation, Visualization

MN – Data curation, Formal Analysis, Investigation, Software, Writing – original draft

SB – Investigation, Supervision, Validation, Visualization, Writing – review & editing

RRM – Investigation, Supervision, Validation, Visualization, Writing – review & editing

SG – Data curation, Funding acquisition, Formal Analysis, Investigation, Methodology, Software, Supervision, Validation, Visualization, Writing – review & editing

TR – Conceptualization, Funding acquisition, Investigation, Methodology, Project administration, Resources, Software, Supervision, Validation, Visualization, Writing – review & editing

Conflicts of interest

There are no conflicts to declare

Research data Statement

All data can be accessed from https://doi.org/10.5281/zenodo.4065552

Acknowledgements

TR acknowledges the financial support provided by Science and Engineering Research Board (SERB), Government of India (SRG/2021/000741) and the Royal Society. SG acknowledge the financial support provided by the UKRI via Grants No. EP/S036180/1 and EP/T024607/1, feasibility study awards to LSBU from the UKRI National Interdisciplinary Circular Economy Hub (EP/V029746/1) and Transforming the Foundation Industries: a Network+ (EP/V026402/1), Royal Academy of Engineering (TSP 1332) and Hubert Curien Alliance Award from the British Council. The work used HPC facilities at BITS Pilani and Isambard Bristol, UK supercomputing service accessed by Resource Allocation Panel (RAP) grant.

References

[1] A.Z. AL Shaqsi, K. Sopian, A. Al-Hinai, Review of energy storage services, applications, limitations, and benefits, Energy Reports. 6 (2020) 288–306. https://doi.org/10.1016/j.egyr.2020.07.028.

[2] Y. Liang, C. Zhao, H. Yuan, Y. Chen, W. Zhang, J. Huang, D. Yu, Y. Liu, M. Titirici, Y. Chueh, H. Yu, Q. Zhang, A review of rechargeable batteries for portable electronic devices, InfoMat. 1 (2019) 6–32. https://doi.org/10.1002/inf2.12000.

[3] Y. Barsukov, J. Qian, Battery Power Management for Portable Devices, Artech House, 2013.

[4] S. Iqbal, H. Khatoon, A. Hussain Pandit, S. Ahmad, Recent development of carbon based materials for energy storage devices, Mater. Sci. Energy Technol. 2 (2019) 417–428. https://doi.org/10.1016/j.mset.2019.04.006.

[5] M.S. Soffian, F.Z. Abdul Halim, F. Aziz, M. A. Rahman, M.A. Mohamed Amin, D.N. Awang Chee, Carbon-based material derived from biomass waste for wastewater treatment, Environ. Adv. 9 (2022) 100259. https://doi.org/10.1016/j.envadv.2022.100259.

[6] M.M. Sabzehmeidani, S. Mahnaee, M. Ghaedi, H. Heidari, V.A.L. Roy, Carbon based materials: a review of adsorbents for inorganic and organic compounds, Mater. Adv. 2 (2021) 598–627. https://doi.org/10.1039/D0MA00087F.

[7] E. Masika, R. Mokaya, Hydrogen Storage in High Surface Area Carbons with Identical Surface Areas but Different Pore Sizes: Direct Demonstration of the Effects of Pore Size, J. Phys. Chem. C. 116 (2012) 25734–25740. https://doi.org/10.1021/jp3100365.

[8] M.I. Maulana Kusdhany, S.M. Lyth, New insights into hydrogen uptake on porous carbon materials via explainable machine learning, Carbon N. Y. 179 (2021) 190–201. https://doi.org/10.1016/j.carbon.2021.04.036.

[9] A. Vergara-Rubio, L. Ribba, D.E. Picón Borregales, K. Sapag, R. Candal, S. Goyanes, Ultramicroporous Carbon Nanofibrous Mats for Hydrogen Storage, ACS Appl. Nano Mater. 5 (2022) 15353–15361. https://doi.org/10.1021/acsanm.2c03401.

[10] M. Bosch, H.-C. Zhou, Porous Carbons for Hydrogen Storage, in: Nanostructured Mater. Next-Generation Energy Storage Convers., Springer Berlin Heidelberg, Berlin, Heidelberg, 2017: pp. 171–202. https://doi.org/10.1007/978-3-662-53514-1_6.

[11] S.L. Candelaria, Y. Shao, W. Zhou, X. Li, J. Xiao, J.-G. Zhang, Y. Wang, J. Liu, J. Li, G. Cao, Nanostructured carbon for energy storage and conversion, Nano Energy. 1 (2012) 195–220. https://doi.org/10.1016/j.nanoen.2011.11.006.

[12] J. Castro-Gutiérrez, A. Celzard, V. Fierro, Energy Storage in Supercapacitors: Focus on Tannin-Derived Carbon Electrodes, Front. Mater. 7 (2020). https://doi.org/10.3389/fmats.2020.00217.

[13] S. Rajagopal, R. Pulapparambil Vallikkattil, M. Mohamed Ibrahim, D.G. Velev, Electrode Materials for Supercapacitors in Hybrid Electric Vehicles: Challenges and Current Progress, Condens. Matter. 7 (2022) 6. https://doi.org/10.3390/condmat7010006.

[14] M. ben ben Mosbah, L. Mechi, R. Khiari, Y. Moussaoui, Current State of Porous Carbon for Wastewater Treatment, Processes. 8 (2020) 1651. https://doi.org/10.3390/pr8121651.

[15] B. Pal, S. Yang, S. Ramesh, V. Thangadurai, R. Jose, Electrolyte selection for supercapacitive devices: a critical review, Nanoscale Adv. 1 (2019) 3807–3835. https://doi.org/10.1039/C9NA00374F.

[16] L. Chen, T. Ji, L. Mu, Y. Shi, H. Wang, J. Zhu, Pore size dependent molecular adsorption of cationic dye in biomass derived hierarchically porous carbon, J. Environ. Manage. 196 (2017) 168–177. https://doi.org/10.1016/j.jenvman.2017.03.013.

[17] T. Liu, G. Liu, Porous organic materials offer vast future opportunities, Nat. Commun. 11 (2020) 4984. https://doi.org/10.1038/s41467-020-15911-8.

[18] P. Zhu, P.R. Slater, E. Kendrick, Insights into architecture, design and manufacture of electrodes for lithium-ion batteries, Mater. Des. 223 (2022) 111208. https://doi.org/10.1016/j.matdes.2022.111208.

[19] Z. Pan, J. Yang, J. Kong, X.J. Loh, J. Wang, Z. Liu, “Porous and Yet Dense” Electrodes for High-Volumetric-Performance Electrochemical Capacitors: Principles, Advances, and Challenges, Adv. Sci. 9 (2022) 2103953. https://doi.org/10.1002/advs.202103953.

[20] V.S. Bhat, S. S, T.J. Jayeoye, T. Rujiralai, U. Sirimahachai, K.F. Chong, G. Hegde, Influence of surface properties on electro-chemical supercapacitors utilizing Callerya atropurpurea pod derived porous nanocarbons: Structure property relationship between porous structures to energy storage devices, Nano Sel. 1 (2020) 226–243. https://doi.org/10.1002/nano.202000013.

[21] B.X. Medina-Rodriguez, V. Alvarado, Use of Gas Adsorption and Inversion Methods for Shale Pore Structure Characterization, Energies. 14 (2021) 2880. https://doi.org/10.3390/en14102880.

[22] H. Mashhadimoslem, M. Safarzadeh Khosrowshahi, M. Jafari, A. Ghaemi, A. Maleki, Adsorption Equilibrium, Thermodynamic, and Kinetic Study of O 2 /N 2 /CO 2 on Functionalized Granular Activated Carbon, ACS Omega. 7 (2022) 18409–18426. https://doi.org/10.1021/acsomega.2c00673.

[23] S.Z. Naqvi, J. Ramkumar, K.K. Kar, Functionalization of fly ash, in: Handb. Fly Ash, Elsevier, 2022: pp. 35–55. https://doi.org/10.1016/B978-0-12-817686-3.00012-8.

[24] G. Fagerlund, Determination of specific surface by the BET method, Matériaux Constr. 6 (1973) 239–245. https://doi.org/10.1007/BF02479039.

[25] P. Sinha, A. Datar, C. Jeong, X. Deng, Y.G. Chung, L.-C. Lin, Surface Area Determination of Porous Materials Using the Brunauer–Emmett–Teller (BET) Method: Limitations and Improvements, J. Phys. Chem. C. 123 (2019) 20195–20209. https://doi.org/10.1021/acs.jpcc.9b02116.

[26] P.I. Ravikovitch, G.L. Haller, A. V. Neimark, Density functional theory model for calculating pore size distributions: pore structure of nanoporous catalysts, Adv. Colloid Interface Sci. 76–77 (1998) 203–226. https://doi.org/10.1016/S0001-8686(98)00047-5.

[27] M.H. Joo, S.J. Park, S.-M. Hong, C.K. Rhee, D. Kim, G. Ji, S.W. Lee, Y. Sohn, X-ray micro computed tomography and efficient electrochemical recovery of lanthanides on porous carbon cylinder electrodes, Compos. Part B Eng. 231 (2022) 109590. https://doi.org/10.1016/j.compositesb.2021.109590.

[28] L. Magagnin, L. Nobili, P.L. Cavallotti, Metastable zinc–nickel alloys deposited from an

alkaline electrolyte, J. Alloys Compd. 615 (2014) S444–S447. https://doi.org/10.1016/j.jallcom.2014.01.240.

[29] C.T.G. Smith, C.A. Mills, S. Pani, R. Rhodes, J.J. Bailey, S.J. Cooper, T.S. Pathan, V. Stolojan, D.J.L. Brett, P.R. Shearing, S.R.P. Silva, X-ray micro-computed tomography as a non-destructive tool for imaging the uptake of metal nanoparticles by graphene-based 3D carbon structures, Nanoscale. 11 (2019) 14734–14741. https://doi.org/10.1039/C9NR03056E.

[30] J. Le Houx, D. Kramer, Physics based modelling of porous lithium ion battery electrodes—A review, Energy Reports. 6 (2020) 1–9. https://doi.org/10.1016/j.egyr.2020.02.021.

[31] K. Kirchner, T. Kirchner, V. Ivaništšev, M.V. Fedorov, Electrical double layer in ionic liquids: Structural transitions from multilayer to monolayer structure at the interface, Electrochim. Acta. 110 (2013) 762–771. https://doi.org/10.1016/j.electacta.2013.05.049.

[32] Y. Zhou, H. Wang, Molecular Dynamics Simulation of a Single Carbon Chain through an Asymmetric Double-Layer Graphene Nanopore for Prolonging the Translocation Time, ACS Omega. 7 (2022) 16422–16429. https://doi.org/10.1021/acsomega.2c00438.

[33] P. Vélez, G.L. Luque, D.E. Barraco, A.A. Franco, E.P.M. Leiva, Pore size distribution of carbon black: An approach from a coarse-grained potential, Comput. Mater. Sci. 209 (2022) 111409. https://doi.org/10.1016/j.commatsci.2022.111409.

[34] Q. Cai, A. Buts, N.A. Seaton, M.J. Biggs, A pore network model for diffusion in nanoporous carbons: Validation by molecular dynamics simulation, Chem. Eng. Sci. 63 (2008) 3319–3327. https://doi.org/10.1016/j.ces.2008.03.032.

[35] J. Wang, C.L. Liu, Molecular Dynamics Simulation for Temperature and Graphite-Like Structure Effects on Amorphous Carbon Graphitization, Mater. Sci. Forum. 956 (2019) 78–86. https://doi.org/10.4028/www.scientific.net/MSF.956.78.

[36] Z. Bo, C. Li, H. Yang, K. Ostrikov, J. Yan, K. Cen, Design of Supercapacitor Electrodes Using Molecular Dynamics Simulations, Nano-Micro Lett. 10 (2018) 33. https://doi.org/10.1007/s40820-018-0188-2.

[37] A. Khaitan, A. Owhal, S.U. Belgamwar, R. Raman Mishra, S. Goel, T. Roy, Designing porous electrode structures for supercapacitors using quenched MD simulations, Mater. Today Proc. (2022). https://doi.org/10.1016/j.matpr.2022.03.726.

[38] S.J. Stuart, A.B. Tutein, J.A. Harrison, A reactive potential for hydrocarbons with intermolecular interactions, J. Chem. Phys. 112 (2000) 6472–6486. https://doi.org/10.1063/1.481208.

[39] C. Qian, B. McLean, D. Hedman, F. Ding, A comprehensive assessment of empirical potentials for carbon materials, APL Mater. 9 (2021) 061102. https://doi.org/10.1063/5.0052870.

[40] V.L. Deringer, G. Csányi, Machine learning based interatomic potential for amorphous carbon, Phys. Rev. B. 95 (2017) 094203. https://doi.org/10.1103/PhysRevB.95.094203.

[41] P. Ranjan, A. Owhal, D. Chakrabarti, S.U. Belgamwar, T. Roy, R. Balasubramaniam, Fundamental insights of mechanical polishing on polycrystalline Cu through molecular dynamics simulations, Mater. Today Commun. 32 (2022) 103980. https://doi.org/10.1016/j.mtcomm.2022.103980.

[42] K. Vollmayr-Lee, Introduction to molecular dynamics simulations, Am. J. Phys. 88 (2020) 401–422. https://doi.org/10.1119/10.0000654.

[43] A. Stukowski, V. V. Bulatov, A. Arsenlis, Automated identification and indexing of dislocations in crystal interfaces, Model. Simul. Mater. Sci. Eng. 20 (2012) 085007. https://doi.org/10.1088/0965-0393/20/8/085007.

[44] H. Tachikawa, T. Iyama, Mechanism of Hydrogen Storage in the Graphene Nanoflake–Lithium–H 2 System, J. Phys. Chem. C. 123 (2019) 8709–8716. https://doi.org/10.1021/acs.jpcc.9b01152.

[45] R. Bardestani, G.S. Patience, S. Kaliaguine, Experimental methods in chemical engineering: specific surface area and pore size distribution measurements—BET, BJH, and DFT, Can. J. Chem. Eng. 97 (2019) 2781–2791. https://doi.org/10.1002/cjce.23632.

[46] A. Torres-Knoop, A. Poursaeidesfahani, T.J.H. Vlugt, D. Dubbeldam, Behavior of the Enthalpy of Adsorption in Nanoporous Materials Close to Saturation Conditions, J. Chem. Theory Comput. 13 (2017) 3326–3339. https://doi.org/10.1021/acs.jctc.6b01193.

[47] Q. Xiong, T.G. Baychev, A.P. Jivkov, Review of pore network modelling of porous media: Experimental characterisations, network constructions and applications to reactive transport, J. Contam. Hydrol. 192 (2016) 101–117. https://doi.org/10.1016/j.jconhyd.2016.07.002.

[48] L. Gong, L. Nie, Y. Xu, Geometrical and Topological Analysis of Pore Space in

Sandstones Based on X-ray Computed Tomography, Energies. 13 (2020) 3774. https://doi.org/10.3390/en13153774.

[49] S. Wang, D. Minami, K. Kaneko, Comparative pore structure analysis of highly porous graphene monoliths treated at different temperatures with adsorption of N2 at 77.4 K and of Ar at 87.3 K and 77.4 K, Microporous Mesoporous Mater. 209 (2015) 72–78. https://doi.org/10.1016/j.micromeso.2015.01.014.

[50] K. Kodera, Y. Onishi, The Molecular Cross-sectional Areas for the Determination of Specific Surface Areas of Solids. I. Carbon Black, Bull. Chem. Soc. Jpn. 32 (1959) 356–361. https://doi.org/10.1246/bcsj.32.356.

[51] J. Zou, C. Fan, Y. Jiang, X. Liu, W. Zhou, H. Xu, L. Huang, A preliminary study on assessing the Brunauer-Emmett-Teller analysis for disordered carbonaceous materials, Microporous Mesoporous Mater. 327 (2021) 111411. https://doi.org/10.1016/j.micromeso.2021.111411.

[52] C. de Tomas, I. Suarez-Martinez, F. Vallejos-Burgos, M.J. López, K. Kaneko, N.A. Marks, Structural prediction of graphitization and porosity in carbide-derived carbons, Carbon N. Y. 119 (2017) 1–9. https://doi.org/10.1016/j.carbon.2017.04.004.

[53] T.B. Shiell, D.G. McCulloch, J.E. Bradby, B. Haberl, D.R. McKenzie, Neutron diffraction discriminates between models for the nanoarchitecture of graphene sheets in glassy carbon, J. Non. Cryst. Solids. 554 (2021) 120610. https://doi.org/10.1016/j.jnoncrysol.2020.120610.

[54] M. Thompson, B. Dyatkin, H.-W. Wang, C. Turner, X. Sang, R. Unocic, C. Iacovella, Y. Gogotsi, A. van Duin, P. Cummings, An Atomistic Carbide-Derived Carbon Model Generated Using ReaxFF-Based Quenched Molecular Dynamics, C. 3 (2017) 32. https://doi.org/10.3390/c3040032.

[55] C. de Tomas, I. Suarez-Martinez, N.A. Marks, Carbide-derived carbons for dense and tunable 3D graphene networks, Appl. Phys. Lett. 112 (2018) 251907. https://doi.org/10.1063/1.5030136.

[56] T.B. Shiell, S. Wong, W. Yang, C.A. Tanner, B. Haberl, R.G. Elliman, D.R. McKenzie, D.G. McCulloch, J.E. Bradby, The composition, structure and properties of four different glassy carbons, J. Non. Cryst. Solids. 522 (2019) 119561. https://doi.org/10.1016/j.jnoncrysol.2019.119561.

[57] J.C. Palmer, A. Llobet, S.-H. Yeon, J.E. Fischer, Y. Shi, Y. Gogotsi, K.E. Gubbins, Modeling the structural evolution of carbide-derived carbons using quenched molecular dynamics, Carbon N. Y. 48 (2010) 1116–1123. https://doi.org/10.1016/j.carbon.2009.11.033.

[58] L.D. Gelb, K.E. Gubbins, Characterization of Porous Glasses: Simulation Models, Adsorption Isotherms, and the Brunauer−Emmett−Teller Analysis Method, Langmuir. 14 (1998) 2097–2111. https://doi.org/10.1021/la9710379.

[59] K. Hormann, V. Baranau, D. Hlushkou, A. Höltzel, U. Tallarek, Topological analysis of non-granular, disordered porous media: determination of pore connectivity, pore coordination, and geometric tortuosity in physically reconstructed silica monoliths, New J. Chem. 40 (2016) 4187–4199. https://doi.org/10.1039/C5NJ02814K.

[60] H.-M. Lee, H.-R. Kang, K.-H. An, H.-G. Kim, B.-J. Kim, Comparative studies of porous carbon nanofibers by various activation methods, Carbon Lett. 14 (2013) 180–185. https://doi.org/10.5714/CL.2013.14.3.180.

[61] E.M. Mistar, T. Alfatah, M.D. Supardan, Synthesis and characterization of activated carbon from Bambusa vulgaris striata using two-step KOH activation, J. Mater. Res. Technol. 9 (2020) 6278–6286. https://doi.org/10.1016/j.jmrt.2020.03.041.

[62] F. Ambroz, T.J. Macdonald, V. Martis, I.P. Parkin, Evaluation of the BET Theory for the Characterization of Meso and Microporous MOFs, Small Methods. 2 (2018) 1800173. https://doi.org/10.1002/smtd.201800173.

[63] M.S. Khosrowshahi, M.A. Abdol, H. Mashhadimoslem, E. Khakpour, H.B.M. Emrooz, S. Sadeghzadeh, A. Ghaemi, The role of surface chemistry on CO2 adsorption in biomass-derived porous carbons by experimental results and molecular dynamics simulations, Sci. Rep. 12 (2022) 8917. https://doi.org/10.1038/s41598-022-12596-5.